PHOTONICS Research

Integrated scanning spectrometer with a tunable micro-ring resonator and an arrayed waveguide grating

Zunyue Zhang,[1] Yi Wang,[1] Jiarui Wang,[2] Dan Yi,[1] David Weng U Chan,[1] Wu Yuan,[2] AND Hon Ki Tsang[1,*]

[1]Department of Electronic Engineering, The Chinese University of Hong Kong, Hong Kong, China
[2]Department of Biomedical Engineering, The Chinese University of Hong Kong, Hong Kong, China
*Corresponding author: hktsang@ee.cuhk.edu.hk

Integrated spectrometers with both wide optical bandwidths and high spectral resolutions are required in applications such as spectral domain optical coherence tomography (SD-OCT). Here we propose a compact integrated scanning spectrometer by using a tunable micro-ring resonator (MRR) integrated with a single arrayed waveguide grating for operation in the 1265–1335-nm range. The spectral resolution of the spectrometer is determined by the quality factor of the MRR, and the optical bandwidth is defined by the free spectral range of the arrayed waveguide grating. The spectrometer is integrated with on-chip germanium photodetectors, which enable direct electrical readout. A 70-nm optical bandwidth and a 0.2-nm channel spacing enabled by scanning the MRR across one free spectral range are demonstrated, which offer a total of 350 wavelength channels with 31-kHz wavelength scanning speed. The integrated spectrometer is applied to measure different spectra and the interference signals from an SD-OCT system, which shows its great potential for future applications in sensing and imaging systems. © 2022 Chinese Laser Press

https://doi.org/10.1364/PRJ.443039

1. INTRODUCTION

Motivated by their many applications in optical communications [1,2] and spectroscopy in chemistry [3,4], biology [5,6], astronomy [7,8], and 3D imaging [9,10], integrated optical spectrometers have attracted widespread research interest [11] because they have the advantages of compact footprints and potentially low cost when manufactured in large volumes, they can be designed to operate with wide optical bandwidths and high spectral resolutions, and they can be integrated with photodetectors that provide a direct electrical readout of optical spectra. Fourier transform (FT) spectrometers, which rely on the FT of the interferograms formed by the unbalanced Mach–Zehnder interferometer (MZI) array, have been demonstrated to have sub-nanometer spectral resolution [12,13]. Spectrometers based on dispersive devices, such as echelle gratings [14,15], arrayed waveguide gratings (AWGs) [16–19], angled multimode interferometers (AMMIs) [20,21], and photonic crystal [22,23], have been extensively studied. However, obtaining high spectral resolution and a large channel count with these conventional spectrometers still poses a difficulty because the spectral resolution is typically proportional to the optical path length. Large device areas become unavoidable for

such spectrometers to attain high resolution. The increased device area, apart from increasing cost, also introduces excess insertion loss, and places a stringent requirement on the uniformity of the thickness and width of the waveguides across the wafer to avoid the crosstalk that typically degrades the performance of integrated spectrometers fabricated on high refractive index contrast waveguide platforms [24]. For example, for an AWG with high resolving power of 10,000, the tolerance on the waveguide width is about 4–5 nm, and thickness variation of less than 1 nm is needed to achieve a phase error of under 120° [25]. Speckle spectrometers, which use wavelength-dependent speckle patterns as fingerprints of input spectra, offer the possibility to obtain high spectral resolution within a small device footprint [26–29]. However, they require precise calibration before spectrum measurement and time-consuming post data processing to retrieve the measured spectra from the speckle patterns.

The tandem configuration of two-stage spectrometers has been previously proposed as an approach to achieve both high spectral resolution and wide optical bandwidth within a single spectrometer. Cascaded two-stage AWG spectrometers have been demonstrated to expand the optical bandwidth and

increase the channel count [30,31]. However, practical results on spectral resolutions are limited by the difficulty in fabricating high-resolution AWG, which requires a relatively large optical phase array. The typical manufacturing process available from commercial foundries offering high refractive index contrast integration platforms does not have sufficient uniformity of the waveguide layer thickness across the wafer, and large cross talk is typically introduced by the nanometer scale deviations in waveguide layer thickness across the large area of the high-resolution stage [25,32]. Micro-ring resonators (MRRs) have been proposed as an alternative of the high-resolution AWG to offer high spectral resolution within an ultracompact footprint [33–35]. However, when the free spectral range (FSR) of the MRR is not equal to the AWG channel spacing [33], a more complicated calibration process and post data processing are necessary to retrieve the spectrum, which increases the complexity of the spectrometer to be used in the bioimaging system, while in previous applications of biosensors [34], it was not necessary to have wide optical bandwidth. We previously demonstrated a stationary spectrometer by using a tandem configuration of interleaved MRRs and multiple identical AWGs [36]. That work formed an integrated spectrometer by using low-resolution AWGs as the secondary stage and multiple parallel MRRs as the primary stage to achieve both high resolution, determined by the quality factor of the MRR, and a wide optical bandwidth, determined by FSR of the AWG [37]. However, precise control of the resonances of multiple MRRs would require either precise heater control of each MRR or additional fabrication processes such as ion implantation and precise annealing to trim the precise position of the wavelength resonances of each MRR [38].

In this paper, we describe an alternative architecture of a scanning spectrometer that does not require precise trimming of the MRR. We use a scanning MRR as the primary stage and a single low-resolution AWG as the secondary stage, as illustrated in Fig. 1. We take advantage of the cyclical nature of the MRR, that is, the wavelengths separated by one FSR of the MRR will be dropped from the output port simultaneously. These dropped wavelengths will then be discriminated by the secondary-stage AWG if the channel spacing of the AWG is designed to match the FSR of the MRR. The resistive electrical heater integrated above the MRR enables the resonance
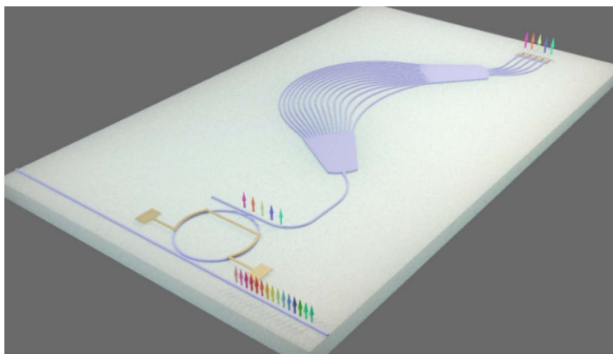

Fig. 1. Schematic of the integrated scanning spectrometer with tunable MRR and a single AWG. Direct electrical readout is enabled by on-chip germanium photodetectors.

wavelength scanning of the MRR across its full FSR. The wavelength scanning of the integrated spectrometer in the full wavelength range can thus be obtained. The proof-of-concept demonstration is implemented on a silicon on insulator (SOI) platform for operation in the 1265–1335-nm wavelength range. This wavelength range was chosen as the near infrared (NIR) optical tissue window for *in vivo* bioimaging applications [39,40]. The integrated spectrometer is demonstrated to have a 70-nm optical bandwidth and a 0.2-nm channel spacing. To our knowledge, this is the widest bandwidth high-resolution integrated spectrometer in the 1300-nm wavelength region, and it is also the one with the most compact footprint. The step-response speed of the heaters used in tuning the MRR corresponds to maximum scanning speed of 31 kHz. The spectrometer is integrated with germanium photodetectors, which enable the direct electrical readout of the spectrometer. No extensive post data processing, beyond the simple initial calibration to remove the wavelength dependence of the insertion losses, is needed. This integrated spectrometer is suitable for measuring different spectra at the scanning speed of the MRR and can capture wideband spectra with high spectral resolution for use in 3D optical coherence tomography (OCT) imaging systems.

2. DEVICE DESIGN AND SIMULATION

The integrated spectrometer is designed for the SOI platform with a 220-nm-thick silicon waveguide layer and 3-μm-thick buried oxide and oxide cladding, and for the transverse electric (TE) mode. The MRR is designed to use 130-nm shallow etched waveguide with 410-nm waveguide width to ensure single mode transmission. The waveguide dimension is illustrated in Fig. 2(a), and the mode profile of the waveguide is shown in Fig. 2(b). The directional coupler is formed by bending waveguides, as illustrated in Fig. 2(c). With the proper design of the bending angle and the gap between the ring and the bus waveguide, the dispersion in the directional coupler can be engineered to enable a uniform coupling ratio and thus meet the critical coupling requirement in the full 70-nm operating wavelength range [41]. The bending angle of the directional coupler is designed to be 10°, and the gap is designed to be 200 nm. The 3D finite-difference time-domain (FDTD) simulation result of the directional coupler is shown in Fig. 2(d). The coupling efficiency is simulated to be about 10% at the center wavelength. The bending radius of the MRR is designed to be 9.28 μm, which fixes the FSR to be 7 nm. The transmission spectrum of the MRR from the drop port may be described by [42]

$$I = \frac{(1-t^2)^2 \alpha}{1 + \alpha^2 t^4 - 2\alpha t^2 \cos\left[\frac{4\pi^2 n_{\text{eff}}(\lambda)r}{\lambda}\right]}, \tag{1}$$

where t is the self-coupling coefficient of the directional coupler, α is the round-trip transmission, n_{eff} is the effective index of the waveguide, which is wavelength dependent due to the waveguide dispersion, λ is the wavelength, and r is the bending radius. A self-coupling coefficient of 0.91 and a round-trip transmission of 0.96 are used in the spectrum calculation.
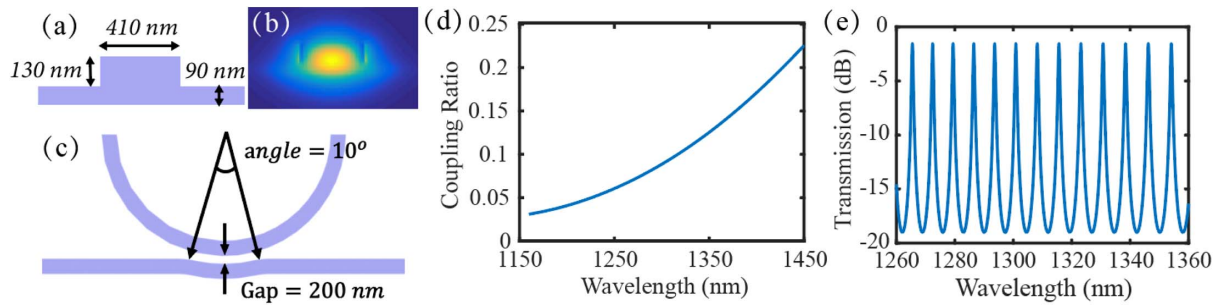
Fig. 2. (a) Waveguide dimension of the MRR. (b) Mode profile in the shallow etched waveguide. (c) Schematic of the bending-shaped directional coupler used in the MRR. (d) Simulated coupling ratio of the designed directional coupler by 3D FDTD simulation. (e) Calculated transmission spectrum of the designed MRR.

The calculated transmission spectrum of the MRR is shown in Fig. 2(e). The extinction ratio is calculated to be about 17.5 dB, and the insertion loss is calculated to be 1.5 dB. An electrical resistive micro-heater is designed above the MRR to enable the resonance wavelength scanning of the ring by the thermo-optic effect, as illustrated in Fig. 1. The width of the heater is designed to be 2.6 μm, and the length of the heater is 53 μm, with a design resistance of 300 Ω.

The channel spacing of the secondary-stage AWG is designed to equal the FSR of the primary-stage MRR, that is, 7 nm. The AWG is designed to have 10 output channels and thus should have an FSR of 70 nm. The waveguide length increment of the waveguide array can be calculated by [43]

$$\Delta L = \frac{\lambda_0^2}{N_g \Delta \lambda_{\mathrm{FSR}}}, \qquad (2)$$

where λ_0 is the center wavelength, N_g is the group index, and $\Delta \lambda_{\mathrm{FSR}}$ is the FSR of the AWG; 800-nm wide fully etched waveguides are used in the waveguide array to reduce the overlap between the waveguide mode and waveguide sidewall. Parabolic tapers with lengths of 5 μm are designed at the interface of slab waveguide and the channel waveguides to reduce transition loss. The minimum bending radius of the arrayed waveguides is designed to be 50 μm to avoid the excitation of the high order waveguide modes and reduce radiation loss. The numerically calculated power coupling between TE_0 mode and TE_1 mode is down to 10^{-6} for the bending radius of 50 μm. The waveguide length increment is calculated to be 5.868 μm, which fixes the FSR to be 70 nm. The length of the free propagation region can be calculated by [43]

$$f_{\mathrm{FPR}} = \frac{n_s d D \lambda_0}{N_g \Delta L \delta \lambda}, \qquad (3)$$

where n_s is the effective index of the slab waveguide, d and D are the pitches of the arrayed waveguides and input/output waveguides, respectively, and $\delta \lambda$ is channel spacing of the AWG, which is designed to be 7 nm. The length of the free propagation region is thus calculated to be 91.28 μm. We use the beam propagation method (BPM) and Kirchhoff–Huygens diffraction formula [44] to simulate the transmission spectrum of the 10-channel AWG. The simulated result is shown in Fig. 3. The channel spacing is simulated to be
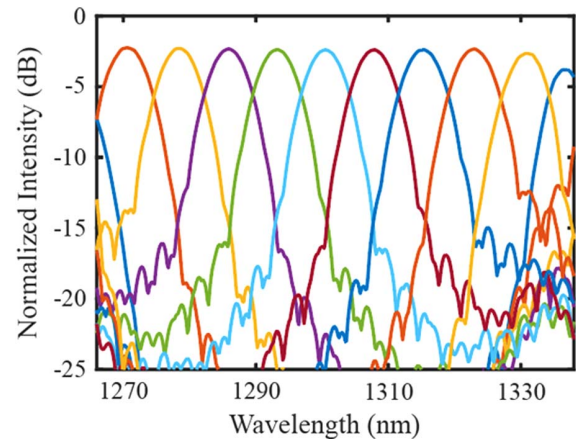

Fig. 3. Simulated transmission spectrum of the 10-channel AWG.

7 nm. The designed AWG has 1.9-dB insertion loss, which is composed of the transition loss at the interface of the slab waveguide and the channel waveguides (1.3 dB), the diffraction field truncation loss at the edges of the arrayed waveguides (0.4 dB), and the insertion loss of the parabolic tapers (0.2 dB).

3. EXPERIMENTAL RESULTS

The integrated spectrometer was fabricated in a multi-project wafer (MPW) by Advanced Micro Foundry Pte Ltd, Singapore (AMF). The microscope image of the whole integrated spectrometer is shown in Fig. 4(a). Figures 4(b) and 4(d) show the microscope images of the 10-channel AWG and the tunable MRR, respectively. The AWG has a footprint of 270 μm × 200 μm. The electrical micro-heater is shown in dark color. Figure 4(c) shows the microscope image of the free propagation region of the AWG with parabolic tapers fabricated at the interface of the slab waveguide and channel waveguides to reduce transition loss. Figure 4(e) shows the microscope image of the integrated germanium photodetectors. Here the standard 28G photodetectors offered by the AMF device library are used [45].

The MRR is characterized by measuring the test structure fabricated on the same chip. The transmission spectrum of the MRR is tested by using an O-band tunable laser and an optical
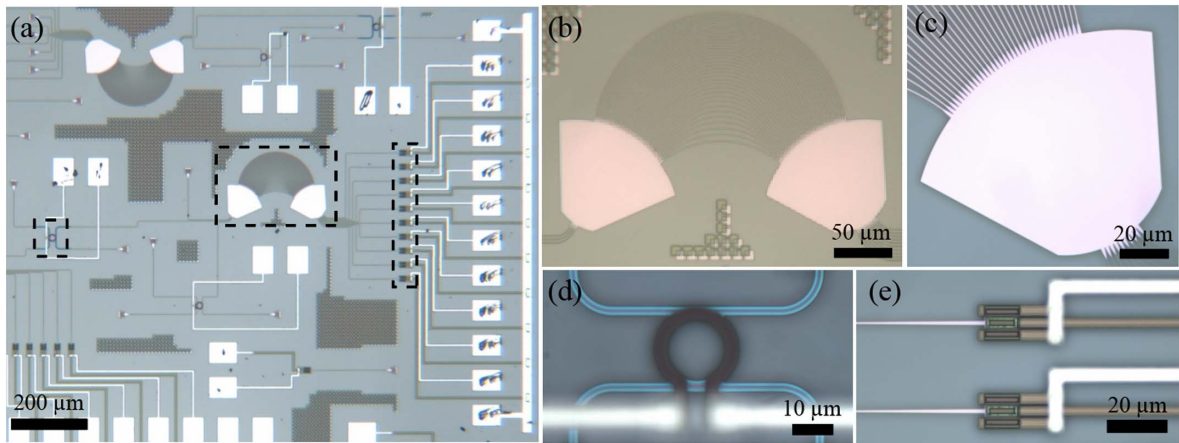
Fig. 4. (a) Microscope image of the integrated spectrometer with heater-controlled tunable MRR, 10-channel AWG, and integrated germanium photodetector array. (b) Microscope image of the 10-channel AWG. (c) Microscope image of the free propagation region of the AWG, with parabolic tapers designed at the interface of the slab waveguide and the channel waveguides. (d) Microscope image of the MRR with electrical micro-heater fabricated above the waveguide. (e) Microscope image of the on-chip germanium photodetector array.

power meter. Light is coupled to the chip and out of the chip through a pair of waveguide grating couplers. The coupling loss of the grating coupler is 6 dB per grating at the center wavelength of 1310 nm. The normalized experimental transmission spectrum of the MRR is shown in Fig. 5(a). The FSR of the MRR is measured to be 7 nm, which agrees with the designed value. The MRR is measured to have 1.6-dB insertion loss. The extinction ratio of the MRR is about 27 dB at the center wavelength and about 20 dB at the off-center wavelength. The non-uniformity in the extinction ratio ascribes to the dispersion in the directional coupler. Figure 5(b) shows the transmission

spectrum within one FSR of the MRR. The 3-dB linewidth of the MRR is measured to be 0.1785 nm.

A maximum voltage of 3.1 V is applied to the micro-heater by a Keithley source meter to perform the resonance wavelength scan of the MRR across the full FSR of 7 nm. The electrical source meter is programmed to serve as a voltage source with 35 voltage steps spaced to increase the electrical power linearly, as shown in Fig. 5(c). The transmission spectrum of the MRR within one FSR during the 35 wavelength scans is shown in Fig. 5(d). There is about 1.5-dB variation in insertion loss during the scans, which is caused by the gradual deviation
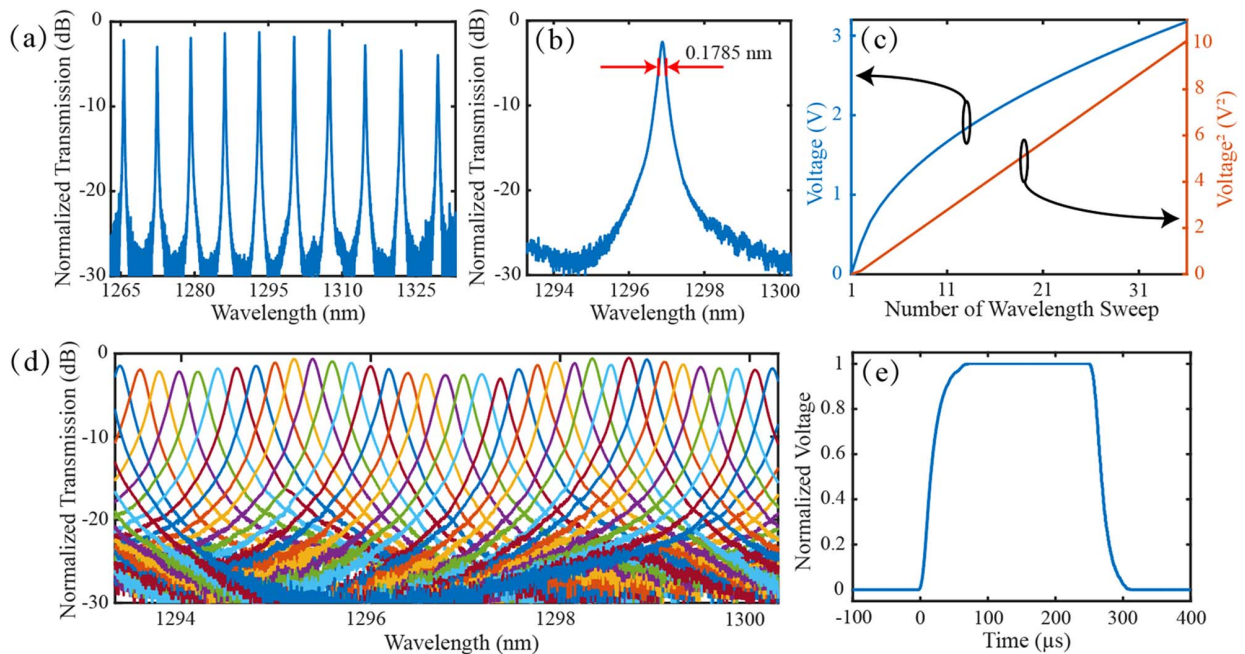

Fig. 5. (a) Normalized experimental transmission spectrum of the MRR. (b) Normalized transmission spectrum within one FSR of the MRR. (c) Voltages applied to the micro-heater for wavelength scans. (d) Normalized experimental transmission spectrum of the MRR with 35 resonance wavelength scans across the full FSR. (e) Step-response measurement result of the MRR with electrical micro-heater.

of the fiber from the optimal position for fiber to chip coupling efficiency over the long duration (∼20 min) measurements of the transmission spectrum of the MRR in the full working wavelength range of the scanning spectrometer with 35 different driving voltages applied to the micro-heater. The electrical resistance of the heater is measured to be 300 Ω. The wavelength tuning efficiency is calculated to be 0.215 nm/mW. The wavelength scanning step of the MRR determines the channel spacing of the integrated spectrometer, which is measured to be 0.2 nm.

The temporal step-response is measured to estimate the wavelength scanning speed that can be offered by the electrical micro-heater. The experimental result is shown in Fig. 5(e). The rise time and fall time are measured to be 32 μs. The maximum wavelength scanning speed can thus be estimated to be 31 kHz. The wavelength scanning speed is mainly limited by the thermo-optic effect. Here the micro-heater is fabricated above the MRR with 2-μm-thick silicon oxide between the ring and heater.

The AWG is characterized by measuring the test structure fabricated on the same chip. The light from the O-band tunable laser is coupled onto the chip through the waveguide grating coupler. The output light is coupled from the chip by the grating coupler to the single mode fiber and sent to the optical power meter for output power measurement.

The normalized transmission spectrum of the 10-channel AWG is shown in Fig. 6. The channel spacing of the AWG is measured to be 7 nm, which agrees with the designed value. A total of 10 output channels covers 70-nm optical bandwidth. The AWG has 2.5-dB experimental insertion loss and −21 dB inter-channel crosstalk at the center wavelength and about −16 dB inter-channel crosstalk at the off-center wavelength channels. The insertion loss of the AWG ascribes to two aspects: transition loss from the slab waveguide to the channel waveguides and power dissipation to the other output channels, which is also the source of inter-channel crosstalk caused by the phase errors in the waveguide array. The higher crosstalk in the off-center channels is limited by the measurement system, as the coupling efficiency of the grating coupler drops at the off-center wavelength range, and the commercial
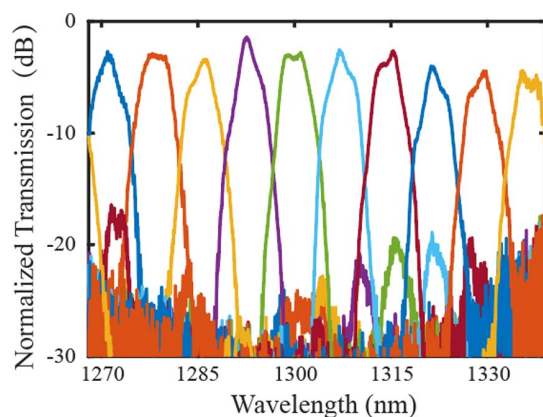
photodetector has a limited dynamic range and cannot measure the channels on the edges with high enough sensitivity.

The two-stage integrated scanning spectrometer is measured by scanning the wavelength of the input light from an O-band tunable laser and measuring the photocurrents from the photodetectors at the output channels simultaneously by a probe array. The input power is 0 dBm, and the responsivity of the photodetector is measured to be 0.5 A/W without bias. The quantum efficiency is thus calculated to be 47.8%. No saturation of the photocurrent is observed during the measurement. The photocurrents measured from the 10 output channels before normalization of the grating coupler spectral response are shown in Fig. 7(a). The loss of the measurement system is about 10 dB at the center wavelength of 1300 nm, which is composed of the 6-dB coupling loss of the input grating coupler and 4-dB insertion loss of the integrated spectrometer. The 4-dB insertion loss of the integrated spectrometer comes from the MRR (1.5 dB) and the AWG (2.5 dB). The wavelength scanning of the integrated spectrometer is obtained by scanning the voltage applied to the micro-heater following the voltage values shown in Fig. 5(c). Figure 7(b) shows the unnormalized transmission spectrum measured from one of the output channels with 35 wavelength scans. The channel spacing, which is determined by the wavelength scanning step, is measured to be 0.2 nm. Figure 7(c) shows the full transmission spectrum including all 350 wavelength channels of the integrated spectrometer measured by the integrated photodetectors before normalization of the grating coupler spectral response. The varied peak insertion loss measured from different AWG channels shown in Fig. 7(c) ascribes to the spectral response of the input grating coupler. The photocurrents measured at the off-center positions of each AWG channel are lower than the peak of the channel due to the envelope of the individual AWG channel. The nonuniformity in the transmission spectrum can be calibrated and compensated if it is needed in practical applications.

As a concept demonstration, we used the proposed integrated scanning spectrometer to measure different spectra formed by two spectral lines from two continuous wave laser sources. The two spectral lines are set to have wavelength spacing of 7 nm, 1 nm, and 0.4 nm. The measurement results are shown in Fig. 8. The two spectral lines are well resolved by the proposed spectrometer, which shows the potential of the integrated scanning spectrometer in measuring wideband spectra with high spectral resolution.

Furthermore, capturing a B-frame by a spectral domain OCT (SD-OCT) system was experimentally demonstrated (Visualization 1). In the initial demonstration, a multilayer dielectric coated aluminum mirror on borosilicate glass substrate was used as the sample. The interference signals from the SD-OCT system were measured by the integrated scanning spectrometer, which is shown in Fig. 9(a). The A-scan result can thus be obtained by conducting FT of the interference signal, as shown in Fig. 9(b). The sample was then scanned by a light beam controlled by a galvo system across a straight line in lateral direction to form a B-frame, which is shown in Fig. 9(c). The B-frame result shows the strong reflection from the metal surface at the depth about 1 mm. (The comparison results
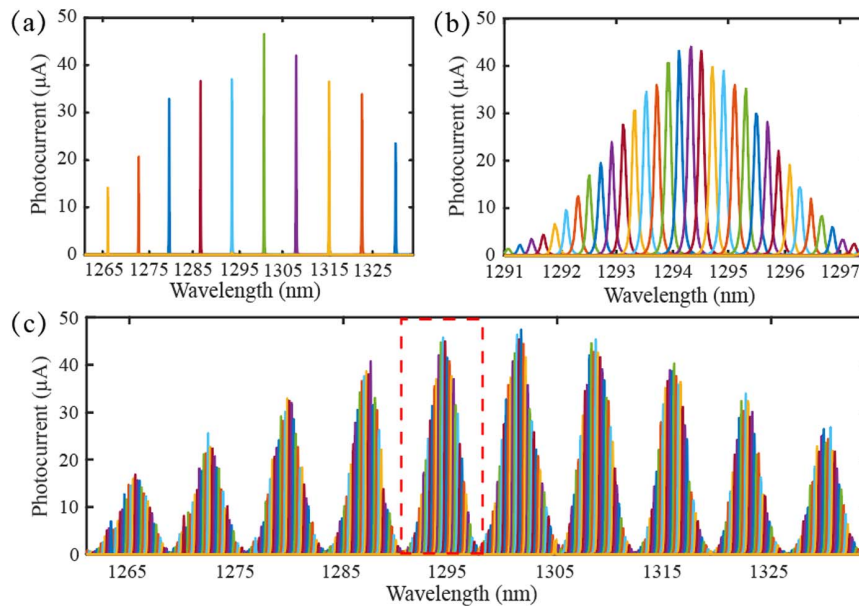

Fig. 6. Normalized experimental transmission spectrum of the 10-channel AWG.

Fig. 7. (a) Unnormalized photocurrents measured from all 10 output channels of secondary-stage AWG without wavelength scans. (b) Unnormalized photocurrents measured from one of the 10 output channels of the AWG with 35 wavelength scans across one AWG channel. (c) Experimental transmission spectrum of the integrated scanning spectrometer with 350 wavelength channels measured by on-chip germanium photodetectors before normalization of the grating coupler spectral response.
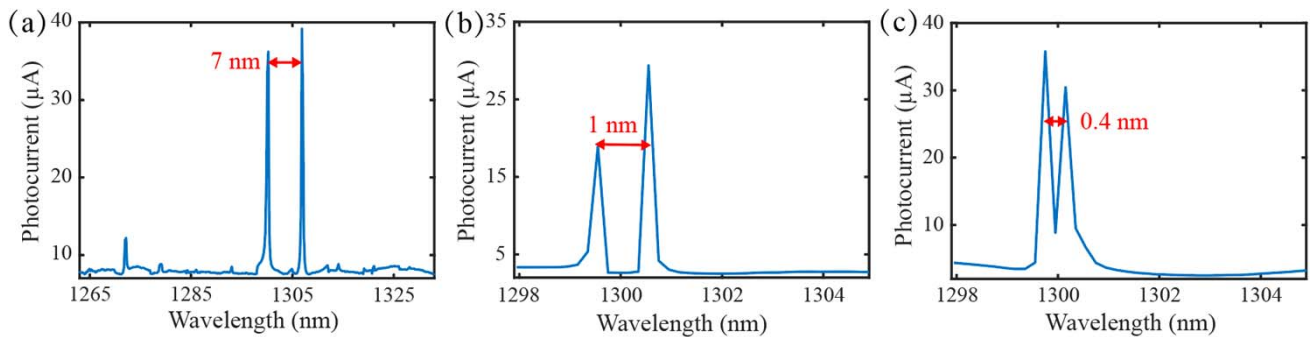

Fig. 8. Measurement results of three different spectra formed by two spectral lines spaced by (a) 7 nm, (b) 1 nm, and (c) 0.4 nm by the proposed integrated scanning spectrometer.

between the spectra measured by a commercial optical spectra analyzer and the integrated scanning spectrometer are shown in Visualization 2.) The multiple lines in the B-frame are caused by multiple reflections in the partially reflective surfaces of the optical coating and the limited optical bandwidth of the spectrometer, as only the central two channels of the spectrometer were used simultaneously during the proof-of-concept demonstration. The axial resolution and image quality
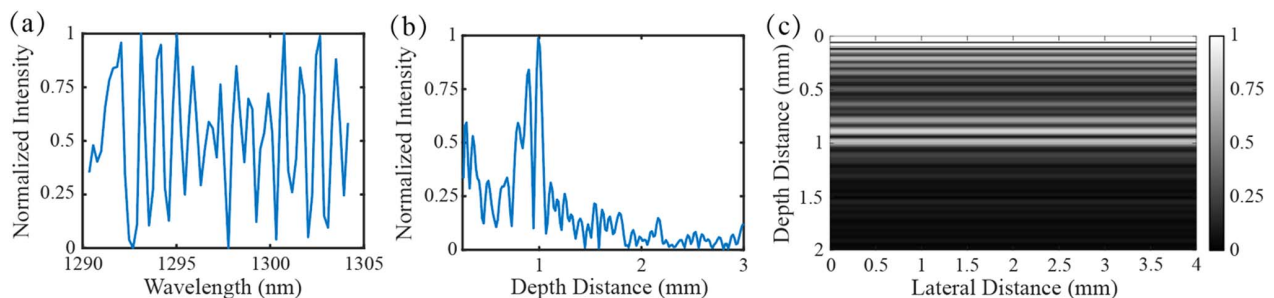

Fig. 9. Experimental demonstration of a B-frame of SD-OCT system. (a) Interference spectrum captured by the proposed scanning spectrometer. (b) A-scan recovered from the measured spectrum. (c) B-frame obtained by scanning the sample across a straight line along the lateral direction.

can be further improved when all wavelength channels are used simultaneously in future work.

4. CONCLUSION

We propose a compact integrated scanning spectrometer by using a tunable MRR with resonance wavelength scan controlled by an electrical micro-heater fabricated above the waveguide and a single 10-channel AWG for operation in 1265–1335-nm wavelength range (NIR optical tissue window). The AWG is designed to have an operation bandwidth of 70 nm, which determines the optical bandwidth of the integrated scanning spectrometer. The channel spacing of the spectrometer is determined by the resonance wavelength scanning step. The narrow linewidth of the MRR ensures high spectral resolution. Continuously increased voltages are applied to the micro-heater to scan the resonance wavelength of the MRR across the full FSR of the MRR. The scanning spectrometer is designed to integrate with on-chip germanium photodetectors. The photocurrents from all 10 output channels of the secondary-stage AWG are measured for each scan. A total of 350 wavelength channels are thus obtained with 0.2-nm channel spacing. The temporal step-response of the MRR with an electrical thermal heater was measured and indicated the maximum wavelength scanning speed of the integrated spectrometer to be 31 kHz. The proposed integrated spectrometer has the potential to measure wideband spectra with high spectral resolution for use in future applications of imaging and sensing systems.

Disclosures. The authors declare no conflicts of interest.

Data Availability. Data underlying the results presented in this paper are not publicly available at this time but may be obtained from the authors upon reasonable request.

REFERENCES

1. H. Toda, T. Yamashita, T. Kuri, and K. Kitayama, "Demultiplexing using an arrayed-waveguide grating for frequency-interleaved DWDM millimeter-wave radio-on-fiber systems," J. Lightwave Technol. **21**, 1735–1741 (2003).
2. C. R. Doerr, L. Zhang, and P. J. Winzer, "Monolithic InP multiwavelength coherent receiver using a chirped arrayed waveguide grating," J. Lightwave Technol. **29**, 536–541 (2011).
3. N. R. Walker, M. J. Linman, M. M. Timmers, S. L. Dean, C. M. Burkett, J. A. Lloyd, J. D. Keelor, B. M. Baughman, and P. L. Edmiston, "Selective detection of gas-phase TNT by integrated optical waveguide spectrometry using molecularly imprinted sol–gel sensing films," Anal. Chim. Acta **593**, 82–91 (2007).
4. C. Tien-Hsin, T. L. Thomas, R. D. Scott, D. R. Scott, F. George, L. Ben, M. Alan, and H. A. Michael, "Compact liquid crystal waveguide based Fourier transform spectrometer for *in-situ* and remote gas and chemical sensing," Proc. SPIE **6977**, 69770P (2008).
5. S. S. Saavedra and W. M. Reichert, "*In situ* quantitation of protein adsorption density by integrated optical waveguide attenuated total reflection spectrometry," Langmuir **7**, 995–999 (1991).
6. B. Brent, K. Pradeep, C. David, and A. Ivan, "Compact low-cost waveguide-based optical spectrometer for detection of chemical/biological agents," Proc. SPIE **8374**, 83740Z (2012).
7. P. Gatkine, S. Veilleux, and M. Dagenais, "Astrophotonic spectrographs," Appl. Sci. **9**, 290 (2019).
8. J. P. Maillard, L. Drissen, F. Grandmont, and S. Thibault, "Integral wide-field spectroscopy in astronomy: the Imaging FTS solution," Exp. Astron. **35**, 527–559 (2013).
9. B. I. Akca, V. D. Nguyen, J. Kalkman, N. Ismail, G. Sengo, F. Sun, A. Driessen, T. G. V. Leeuwen, M. Pollnau, K. Wörhoff, and R. M. D. Ridder, "Toward spectral-domain optical coherence tomography on a chip," IEEE J. Sel. Top. Quantum Electron. **18**, 1223–1233 (2012).
10. E. A. Rank, R. Sentosa, D. J. Harper, M. Salas, A. Gaugutz, D. Seyringer, S. Nevlacsil, A. Maese-Novo, M. Eggeling, P. Muellner, R. Hainberger, M. Sagmeister, J. Kraft, R. A. Leitgeb, and W. Drexler, "Toward optical coherence tomography on a chip: *in vivo* three-dimensional human retinal imaging using photonic integrated circuit-based arrayed waveguide gratings," Light Sci. Appl. **10**, 6 (2021).
11. Z. Yang, T. Albrow-Owen, W. Cai, and T. Hasan, "Miniaturization of optical spectrometers," Science **371**, eabe0722 (2021).
12. M. C. M. M. Souza, A. Grieco, N. C. Frateschi, and Y. Fainman, "Fourier transform spectrometer on silicon with thermo-optic non-linearity and dispersion correction," Nat. Commun. **9**, 665 (2018).
13. A. Li and Y. Fainman, "Integrated silicon Fourier transform spectrometer with broad bandwidth and ultra-high resolution," Laser Photon. Rev. **15**, 2000358 (2021).
14. S. Janz, A. Balakrishnan, S. Charbonneau, P. Cheben, A. Delage, K. Dossou, L. Erickson, M. Gao, P. A. Krug, B. Lamontagne, M. Packirisamy, M. Pearson, and D. Xu, "Planar waveguide echelle gratings in silica-on-silicon," IEEE Photon. Technol. Lett. **16**, 503–505 (2004).
15. X. Ma, M. Li, and J. He, "CMOS-compatible integrated spectrometer based on echelle diffraction grating and MSM photodetector array," IEEE Photon. J. **5**, 6600807 (2013).
16. M. K. Smit, "New focusing and dispersive planar component based on an optical phased array," Electron. Lett. **24**, 385–386 (1988).
17. Z. Zhang, Y. Wang, and H. K. Tsang, "Ultracompact 40-channel arrayed waveguide grating on silicon nitride platform at 860 nm," IEEE J. Quantum Electron. **56**, 8400308 (2020).
18. S. Cheung, T. Su, K. Okamoto, and S. J. B. Yoo, "Ultra-compact silicon photonic 512 × 512 25 GHz arrayed waveguide grating router," IEEE J. Sel. Top. Quantum Electron. **20**, 310–316 (2014).
19. D. Dai, Z. Wang, J. F. Bauters, M. C. Tien, M. J. R. Heck, D. J. Blumenthal, and J. E. Bowers, "Low-loss Si$_3$N$_4$ arrayed-waveguide grating (de)multiplexer using nano-core optical waveguides," Opt. Express **19**, 14130–14136 (2011).
20. T. D. Bucio, A. Z. Khokhar, G. Z. Mashanovich, and F. Y. Gardes, "Athermal silicon nitride angled MMI wavelength division (de)multiplexers for the near-infrared," Opt. Express **25**, 27310–27320 (2017).
21. Y. Hu, R. M. Jenkins, F. Y. Gardes, E. D. Finlayson, G. Z. Mashanovich, and G. T. Reed, "Wavelength division (de)multiplexing based on dispersive self-imaging," Opt. Lett. **36**, 4488–4490 (2011).
22. B. Momeni, E. S. Hosseini, M. Askari, M. Soltani, and A. Adibi, "Integrated photonic crystal spectrometers for sensing applications," Opt. Commun. **282**, 3168–3171 (2009).
23. B. Momeni, E. S. Hosseini, and A. Adibi, "Planar photonic crystal microspectrometers in silicon-nitride for the visible range," Opt. Express **17**, 17060–17069 (2009).
24. Z. Zhang, Y. Wang, and H. K. Tsang, "Experimental study of dependence of waveguide array phase errors on waveguide width," in *Proceedings of Asia Communications and Photonics Conference (ACP)* (IEEE, 2019), pp. 1–3.
25. P. Gatkine, N. Jovanovic, C. Hopgood, S. Ellis, R. Broeke, K. Ławniczuk, J. Jewell, J. K. Wallace, and D. Mawet, "Potential of

commercial SiN MPW platforms for developing mid/high-resolution integrated photonic spectrographs for astronomy," Appl. Opt. **60**, D15–D32 (2021).

26. B. Redding, S. F. Liew, R. Sarma, and H. Cao, "Compact spectrometer based on a disordered photonic chip," Nat. Photonics **7**, 746–751 (2013).

27. B. Redding, S. Fatt Liew, Y. Bromberg, R. Sarma, and H. Cao, "Evanescently coupled multimode spiral spectrometer," Optica **3**, 956–962 (2016).

28. N. K. Metzger, R. Spesyvtsev, G. D. Bruce, B. Miller, G. T. Maker, G. Malcolm, M. Mazilu, and K. Dholakia, "Harnessing speckle for a sub-femtometre resolved broadband wavemeter and laser stabilization," Nat. Commun. **8**, 15610 (2017).

29. Z. Zhang, Y. Li, Y. Wang, Z. Yu, X. Sun, and H. K. Tsang, "Compact high resolution speckle spectrometer by using linear coherent integrated network on silicon nitride platform at 776 nm," Laser Photon. Rev. **15**, 2100039 (2021).

30. B. I. Akca and C. R. Doerr, "Interleaved silicon nitride AWG spectrometers," IEEE Photon. Technol. Lett. **31**, 90–93 (2019).

31. A. van Wijk, C. R. Doerr, Z. Ali, M. Karabiyik, and B. I. Akca, "Compact ultrabroad-bandwidth cascaded arrayed waveguide gratings," Opt. Express **28**, 14618–14626 (2020).

32. A. Stoll, K. Madhav, and M. Roth, "Performance limits of astronomical arrayed waveguide gratings on a silica platform," Opt. Express **28**, 39354–39367 (2020).

33. H. H. Zhu, S. N. Zheng, J. Zou, H. Cai, Z. Y. Li, and A. Q. Liu, "A high-resolution Integrated Spectrometer based on cascaded a ring resonator and an AWG," in *Proceedings of Conference on Lasers and Electro-Optics* (IEEE, 2020), paper JTu2G.32.

34. J. Zou, Z. Le, and J. He, "Temperature self-compensated optical waveguide biosensor based on cascade of ring resonator and arrayed waveguide grating spectrometer," J. Lightwave Technol. **34**, 4856–4863 (2016).

35. G. Yurtsever and R. Baets, "Integrated spectrometer on silicon on insulator," in *Proceedings of 16th Annual Symposium of the IEEE Photonics Benelux Chapter* (IEEE, 2011), pp. 273–276.

36. Z. Zhang, Y. Wang, and H. K. Tsang, "Tandem configuration of microrings and arrayed waveguide gratings for a high-resolution and broadband stationary optical spectrometer at 860 nm," ACS Photon. **8**, 1251–1257 (2021).

37. S. Zheng, H. Cai, J. Song, J. Zou, P. Y. Liu, Z. Lin, D. Kwong, and A. Liu, "A single-chip integrated spectrometer via tunable microring resonator array," IEEE Photon. J. **11**, 6602809 (2019).

38. M. M. Milosevic, X. Chen, W. Cao, D. J. Thomson, G. T. Reed, C. G. Littlejohns, and H. Wang, "Ion implantation in silicon for photonic device trimming," in *Proceedings of Conference on Lasers and Electro-Optics Pacific Rim* (IEEE, 2017), paper s1915.

39. K. Bizheva, B. Považay, B. Hermann, H. Sattmann, W. Drexler, M. Mei, R. Holzwarth, T. Hoelzenbein, V. Wacheck, and H. Pehamberger, "Compact, broad-bandwidth fiber laser for sub-2-μm axial resolution optical coherence tomography in the 1300-nm wavelength region," Opt. Lett. **28**, 707–709 (2003).

40. A. D. Aguirre, N. Nishizawa, J. G. Fujimoto, W. Seitz, M. Lederer, and D. Kopf, "Continuum generation in a novel photonic crystal fiber for ultrahigh resolution optical coherence tomography at 800 nm and 1300 nm," Opt. Express **14**, 1145–1160 (2006).

41. Z. Lu, H. Yun, Y. Wang, Z. Chen, F. Zhang, N. A. F. Jaeger, and L. Chrostowski, "Broadband silicon photonic directional coupler using asymmetric-waveguide based phase control," Opt. Express **23**, 3795–3808 (2015).

42. J. M. Choi, R. K. Lee, and A. Yariv, "Ring fiber resonators based on fused-fiber grating add–drop filters: application to resonator coupling," Opt. Lett. **27**, 1598–1600 (2002).

43. K. Okamoto, "Planar lightwave circuits," in *Fundamentals of Optical Waveguides*, 2nd ed. (Academic, 2006), pp. 417–534.

44. D. Dai, L. Liu, and S. He, "Three-dimensional hybrid modeling based on a beam propagation method and a diffraction formula for an AWG demultiplexer," Opt. Commun. **270**, 195–202 (2007).

45. S. Y. Siew, B. Li, F. Gao, H. Y. Zheng, W. Zhang, P. Guo, S. W. Xie, A. Song, B. Dong, L. W. Luo, C. Li, X. Luo, and G. Q. Lo, "Review of silicon photonics technology and platform development," J. Lightwave Technol. **39**, 4374–4389 (2021).